



On the origin of the elusive first intermediate of CO₂ electroreduction

Irina V. Chernyshova^{a,1}, Ponisseril Somasundaran^a, and Sathish Ponnurangam^b

^aDepartment of Earth and Environmental Engineering, Columbia University, New York, NY 10027; and ^bDepartment of Chemical and Petroleum Engineering, University of Calgary, Calgary, AB, Canada T2N 1N4

Edited by Alexis T. Bell, University of California, Berkeley, CA, and approved August 17, 2018 (received for review February 6, 2018)

We resolve the long-standing controversy about the first step of the CO₂ electroreduction to fuels in aqueous electrolytes by providing direct spectroscopic evidence that the first intermediate of the CO₂ conversion to formate on copper is a carboxylate anion *CO₂⁻ coordinated to the surface through one of its C–O bonds. We identify this intermediate and gain insight into its formation, its chemical and electronic properties, as well as its dependence on the electrode potential by taking advantage of a cutting-edge methodology that includes operando surface-enhanced Raman scattering (SERS) empowered by isotope exchange and electrochemical Stark effects, reaction kinetics (Tafel) analysis, and density functional theory (DFT) simulations. The SERS spectra are measured on an operating Cu surface. These results advance the mechanistic understanding of CO₂ electroreduction and its selectivity to carbon monoxide and formate.

spectroscopy | carbon monoxide | carbonate | adsorption | mechanism

The electrocatalytic conversion of abundant CO₂ to fuels and other useful chemicals has attracted significant interest in the past decade as a promising complementary way to store excessive renewable energy (1, 2). However, commercialization of this green technology is hampered by the absence of a viable catalyst. Even though the catalyst discovery can significantly be accelerated using the emerging approach of computational catalyst design (3), its applicability to CO₂ electroreduction has been limited mostly to explaining experimental trends, rather than to predicting new materials (4–6). This situation roots from a poor mechanistic understanding of this reaction, which starts with a poor understanding of its very first step—activation of CO₂.

In fact, it is currently unclear whether CO₂ electroreduction on different materials starts with one common or several different first intermediates and what their structures are. Specifically, Hori et al. (7, 8) have postulated that, on metals such as Au, Cu, and Ag with medium to high overpotentials for hydrogen evolution reaction (HER), CO₂ is reduced through one common first intermediate, which is carboxylate *CO₂⁻ (* denotes the surface-coordinated state of the ligand):



This first step is supported by the reaction kinetics analysis (7, 9–15).

If so, it is still unclear what the structure of *CO₂⁻ is and how it controls the reaction pathway. As a ligand, CO₂ is very versatile in terms of its coordination to metal centers (16, 17). In the context of CO₂ electroreduction, the most often cited carboxylate structures include η²(O,O)-CO₂⁻ (O,O-down) (18–20), η¹(C)-CO₂⁻ (C-down) (21), and η²(C,O)-CO₂⁻ (C,O-down) (22–24) (Fig. 1). As proposed by Hori et al. (7, 8), strongly adsorbed η¹(C)-CO₂⁻ or η²(C,O)-CO₂⁻ can be converted to CO after they are protonated to carboxyl *COOH (Fig. 1):



which reductively dissociates to CO and H₂O upon proton coupled electron transfer (PCET):



In contrast, the reaction can be directed toward formate if *CO₂⁻ is adsorbed through oxygen(s) or weakly through carbon.

This structure allows the carbon atom to be hydrogenated by either a direct Tafel-like reaction with surface hydride *H,



or by PCET,



An alternative is a more contemporary model that has largely been drawn from density functional theory (DFT) simulations (5, 6, 22, 25, 26). It postulates that CO and formate have different precursors—carboxyl *COOH and O (or O,O)-coordinated formyl *OCHO, respectively (Fig. 1). However, there is no consensus about how these two species are formed. According to Nørskov and coworkers (5, 26), carboxyl and formyl are formed through PCET:



and



respectively. In contrast, Goddard and coworkers (22, 25) adhere to the [1] and [2] pathway for carboxyl, and the hydride transfer (Eley–Rideal) mechanism for formyl:



Significance

The understanding of a catalytic reaction starts with understanding its first elementary step. Surprisingly, despite the large number of studies, it is unclear whether one common or two different first intermediates control the selectivity of CO₂ electroreduction to formate and CO. We settle this controversy for Cu, which is best known for its unique capacity to synthesize C₁₊ products but is just emerging as a superior earth-abundant catalyst for CO and formate. We provide solid experimental and theoretical support of the one common first-intermediate (Hori's) model, the first intermediate being carboxylate. This outcome is an essential milestone toward accurate specification of the reaction descriptors in the growing effort to accelerate the discovery of a viable CO₂ electroreduction catalyst.

Author contributions: I.V.C. designed research; I.V.C. and S.P. performed research; I.V.C. and P.S. contributed new analytic tools; I.V.C. and S.P. analyzed data; I.V.C. conceived the main ideas; P.S. discussed results; and I.V.C. and S.P. wrote the paper.

The authors declare no conflict of interest.

This article is a PNAS Direct Submission.

Published under the PNAS license.

¹To whom correspondence should be addressed. Email: irina905C@gmail.com.

This article contains supporting information online at www.pnas.org/lookup/suppl/doi:10.1073/pnas.1802256115/-DCSupplemental.

Published online September 17, 2018.

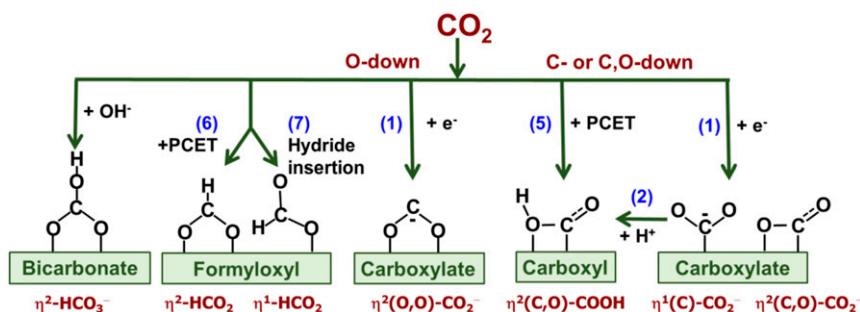


Fig. 1. Possible first intermediates of CO₂ electroreduction in aqueous electrolytes.

The third possibility can be the direct two-electron reduction of adsorbed bicarbonate HCO₃[−] (27, 28).

The aforementioned uncertainty is explained by the phenomenological complexity of CO₂ electroreduction, coupled with intrinsic limitations of the electrochemical and computational methods. Electrochemical surface-enhanced vibrational spectroscopy has not helped much in clarifying this issue either, even though this method has already established itself as a powerful tool to magnify our view of electrified interfaces (29). The only surface species unambiguously identified in aqueous electrolytes on Cu (30–35), Au (14), and Ag (36, 37) is carbon monoxide, while the structure of the other surface species remains highly controversial. This situation stems from the fact that the adsorbate structures have mostly been proposed based on the similarity of their one C–O stretching peak with a peak theoretically predicted or observed in other systems without corroborating by other spectral peaks and the ¹³C/¹²C and D₂O/H₂O isotope exchange effects. This approach is evidently reductionistic as it neglects the strong effects of the catalyst surface, interfacial electric field (including ionic pairing with a counterion), and hydration on the adsorbate spectrum, which can lead to great confusion (38, 39). Moreover, frequencies of the C–O stretching vibrations involve the same CO₂ moiety. Hence, their values are not characteristic of the species shown in Fig. 1. Another source of confusion can be uncontrollable organic contaminations, which can be spotted by the ¹³C/¹²C isotope exchange effect. Finally, to get surface enhancement, the earlier studies have been performed on model roughened surfaces, without validating their catalytic activity. As a result, even if the CO₂-derived adsorbates are identified correctly, it does not warrant that the reaction intermediate is among them because the latter can be formed only on an operating catalyst.

In our study, we focus on Cu because it is one of the most effective pure metal catalysts of CO₂ electroreduction, along with Ag, Pd, and Au (18). At the same time, Cu stands out of this group due to its low cost and unique capacity to synthesize C₁₊ products. The interest in Cu has additionally been elevated by recent findings of its remarkably high efficiency in the synthesis of CO and formate (12, 40, 41)—two of the most feasible targets of the CO₂ conversion technology (2).

Paradoxically, among the large number of studies of CO₂ electroreduction on Cu, only three have attempted to gain insight into the first step of this reaction (12, 22, 26). In particular, Li and Kanan (12) have concluded on the basis of the experimental Tafel slope that the CO synthesis on Cu starts with the formation of carboxylate *CO₂[−] [1]. This result is supported by a quantum chemical study of Goddard and coworkers (22), which predicts that CO₂ is converted to CO on Cu(100) through steps [1]–[3]. In contrast, according to Nørskov and coworkers (26), Cu(111) and Cu(100) prefer to synthesize formate because these surfaces provide a more favorable thermodynamics for the formation of formyloxyl [6] over carboxyl [5]. Thus, the chemical identity of the first intermediate of the CO₂ electroreduction on

Cu and hence the nature of the selectivity of Cu to CO and formate remains elusive.

To bridge this gap, we take advantage of SERS. In contrast to its more often used rival, surface-enhanced infrared absorption spectroscopy (SEIRAS), SERS can be measured on an actual catalyst. In addition, SERS can access a much broader spectral range, which allows for more reliable interpretation of the adsorbate structure. Moreover, SERS spectra are absolute, while SEIRAS spectra are differential and therefore are distorted by the negative peaks of the species present on the electrode surface at the reference potential.

To verify our assignment of SERS peaks, we use the D₂O/H₂O and ¹³C/¹²C isotope exchange, as well as electrochemical Stark effects. The latter presents the shift of the vibrational frequency of the adsorbate with electrode potential. To the first order of the theory, the frequency shift Δν by electric field \vec{F} can be written as $\Delta\nu \approx -|\Delta\vec{\mu}| \cdot |\Delta\vec{F}| \cdot \cos\varphi$, where Δ \vec{F} is the change in the local electric field, Δ $\vec{\mu}$ is the change in the vibrating dipole moment between the ground and first excited vibrational states, and φ is the angle between the vectors of the dipole and the field (42). Hence, the sign of the Stark effect characterizes the orientation of the adsorbate with respect to the applied electric field \vec{F} . A change in the Stark tuning rate (Δν/ΔE, where ΔE is a change in the electrode potential) suggests that the adsorbate or its local environment is perturbed by a certain surface reaction, which can help identify peaks that characterize the same adsorbate. We further corroborate the spectroscopy-based conclusions with the Tafel analysis of the reaction kinetics and with DFT simulations.

Using this advanced approach, we validate Hori's hypothesis that CO₂ electroreduction starts with a common first intermediate, which is carboxylate. We identify the structure of this intermediate as η²(C,O)-CO₂[−], find that it can be formed at potentials significantly anodic of the onset of CO₂ electroreduction, and conclude that the electrocatalytic activity of the metal ties with strengths of the metal–C and metal–O bonds of η²(C,O)-CO₂[−].

Materials and Methods

A roughened Cu electrode was prepared from a 0.5-mm-thick copper foil (99.9985% metals basis) by one oxidation–reduction cycle as reported in *SI Appendix, section S1*. The surface morphology was assessed using SEM (*SI Appendix, Fig. S5*). The roughness factor of 17 ± 3 of the surface was estimated using the dependence of the electric double-layer capacitance on the scan rate in cyclic voltammograms (CVs) (*SI Appendix, Fig. S6*). The surface crystallographic composition, as inferred from the hydroxyl adsorption peaks in CVs, is dominated by the (100), (110), and (111) planes (*SI Appendix, Fig. S7A*). The electrocatalytic activity of the Cu surface was characterized using CVs (*SI Appendix, Fig. S7B*) and preparative electrolysis (*SI Appendix, Fig. S8*). The electrolysis products were measured using NMR and gas chromatography. SERS spectra were acquired in a laboratory-made one-compartment three-electrode spectroelectrochemical cell using a LABRAM-ARAMIS confocal Raman microscope with a HeNe (633-nm) laser. DFT calculations were performed using a plane wave DFT code (The Vienna Ab initio Simulation Package, VASP-5.3.3). Details of the experimental and theoretical methods are provided in *SI Appendix, section S1*.

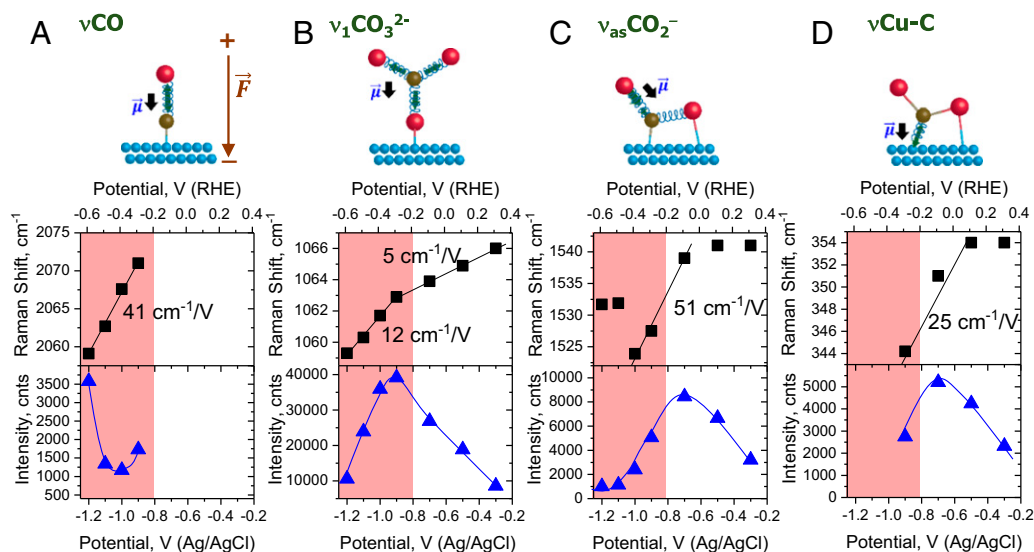


Fig. 3. Effect of electrode potential on the frequencies and intensities of (A) ν_{CO} of $^*\text{CO}$, (B) $\nu_1\text{CO}_3^{2-}$ of $^*\text{CO}_3^{2-}$, (C) $\nu_{\text{as}}\text{CO}_2^-$ of $^*\text{CO}_2^-$ and (D) $\nu_{\text{Cu-C}}$ of $^*\text{CO}_2^-$ in the spectra shown in Fig. 2. The black arrows in the schemes of the corresponding vibrations show the directions of their dipole moments $\vec{\mu}$. \vec{F} is the local (negative) electric field at a negatively charged electrode. The shadowed areas show the region where cathodic current is observed (*SI Appendix, Fig. S7B*). Oxygen is red. Carbon is gray. Copper is blue. The potential is additionally reported vs. the reversible hydrogen electrode (RHE) scale, which is calculated as $E(\text{RHE}) = E(\text{Ag/AgCl}) + 0.209 + 0.059\text{pH}$.

The ν_{CO} peak of $^*\text{CO}$ is subject to the electrochemical Stark effect with a Stark tuning rate of $40 \pm 5 \text{ cm}^{-1}/\text{V}$ (Fig. 3A), typical of CO chemisorbed on atop sites (44, 45). The positive sign of the rate (red shift) reflects that the $\text{C}\equiv\text{O}$ dipole is stretched out by the negative electric field (directed toward the surface) (scheme in Fig. 3A).

To conclude, even though the CO level in the gas phase is below the detection limit, CO is still formed in a small amount on the Cu surface.

Carbonate. At -0.3 V and more negative potentials, the SERS spectra are dominated by a strong peak at $\sim 1,065 \text{ cm}^{-1}$ (Fig. 2). This peak has earlier been detected at $1,050\text{--}1,056 \text{ cm}^{-1}$ on Cu in gas phase (46) and under electrochemical conditions (33–35), where it has been assigned to adsorbed carbonate. Below, we refine the peak assignment to the totally symmetric C–O stretching vibration, $\nu_1\text{CO}_3^{2-}$, of a weakly adsorbed monodentate carbonate $\eta^1\text{-CO}_3^{2-}$ (scheme in Fig. 3B).

To start with, the $1,065\text{-cm}^{-1}$ peak is in the characteristic frequency range of the $\nu_1\text{CO}_3^{2-}$ vibration of carbonate (38, 48, 49). This vibration presents centrosymmetric movements of the CO_3^{2-} oxygen atoms with respect to the central carbon atom (scheme in Fig. 3B). In agreement with this assignment, the $1,065\text{-cm}^{-1}$ peak is negligibly affected by the $^{13}\text{C}/^{12}\text{C}$ and $\text{D}_2\text{O}/\text{H}_2\text{O}$ isotope exchange (Fig. 4 and *SI Appendix, Figs. S16 and S17*).

Next, the dependence of the $\nu_1\text{CO}_3^{2-}$ peak on potential indicates that the carbonate in question is chemisorbed. First, even though the peak intensity decreases, it remains prominent at potentials cathodic of -0.9 V (Fig. 3B). At these potentials, the electrocatalytic current is observed (*SI Appendix, Fig. S7B*) while the Cu surface is expected to be negatively charged (50). Moreover, at potentials from -0.3 to -0.9 V where the Cu surface becomes less positively charged, the peak intensity increases. Another indicator of chemisorption is the susceptibility of the $\nu_1\text{CO}_3^{2-}$ peak to the electrochemical Stark effect (Fig. 3B). Specifically, this peak red shifts at an initial rate of $5 \text{ cm}^{-1}/\text{V}$, which increases stepwise up to $12 \text{ cm}^{-1}/\text{V}$ at -0.9 V . Both the shift and the break are reproduced qualitatively in *SI Appendix, Figs. S12B and S14B*. The Stark shift, which reflects a change in the local electric field of the vibrating dipole, is typically considered as an indicator of the chemisorbed state of an interfacial species (51). The reason is that such a species is exposed to a stronger interfacial electric field than the physisorbed one, which is screened from the electric field by the hydration shell. Chemisorption can also explain why the adsorbed species is CO_3^{2-} while the dominant carbonaceous species in the electrolyte is HCO_3^- .

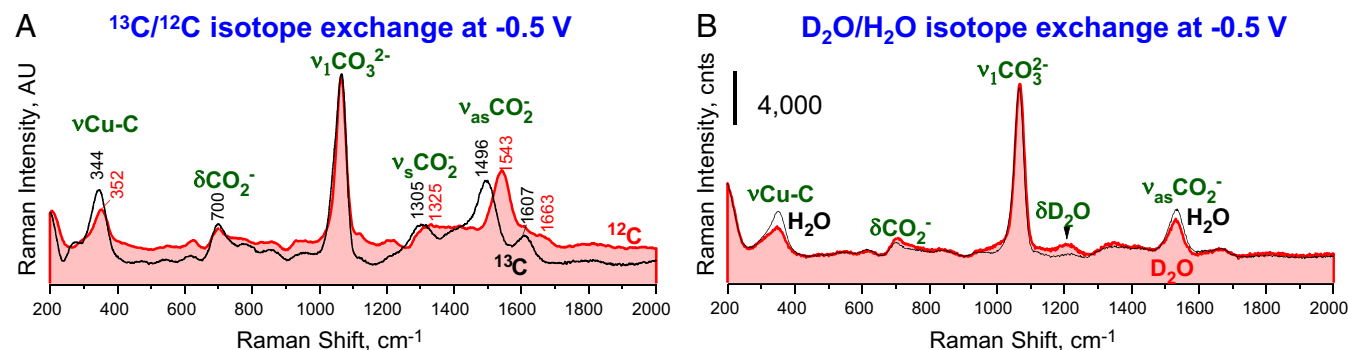


Fig. 4. Effect of the isotope exchange on SERS spectra of species adsorbed on the roughened Cu electrode at -0.5 V (Ag/AgCl) in CO_2 -saturated 0.1 M NaHCO_3 : (A) $^{13}\text{C}/^{12}\text{C}$ exchange and (B) $\text{D}_2\text{O}/\text{H}_2\text{O}$ exchange. Results at -0.3 and -1.1 V are shown in *SI Appendix, Fig. S17*.

Now we look at the position of the $\nu_1\text{CO}_3^{2-}$ peak of the chemisorbed carbonate, which is at 1,060–1,068 cm^{-1} (Fig. 3B). Its proximity to $\nu_1\text{CO}_3^{2-}$ of dissolved carbonate (1,063 cm^{-1}) (SI Appendix, Fig. S18) indicates that the adsorption strength of this carbonate is relatively weak. For comparison, strongly coordinated carbonates with bridging/bidentate and monodentate structures are characterized by $\nu_1\text{CO}_3^{2-}$ below 1,040–1,050 cm^{-1} (38, 48, 49). A similarly weak perturbation of the $\nu_1\text{CO}_3^{2-}$ peak is observed for a carbonate weakly chemisorbed at the Fe(III)(hydr)oxide–water interface (39). This species has a $\eta^1\text{-CO}_3^{2-}$ structure in which the noncoordinated oxygen(s) atom is involved in strong noncovalent interactions (ionic pairing) with a coadsorbed hydrated alkali metal cation or hydronium (39). Hence, it is plausible that the weakly chemisorbed carbonate on Cu has a similar structure.

Apart from the $\nu_1\text{CO}_3^{2-}$ peak, $\eta^1\text{-CO}_3^{2-}$ is expected to generate two $\nu_3\text{C-O}$ peaks that originate from the doubly degenerate C–O stretching vibration $\nu_3\text{CO}_3^{2-}$ at $\sim 1,400\text{ cm}^{-1}$ of free CO_3^{2-} (D_{3h}) (SI Appendix, Fig. S18). We associate these peaks with weak features at 1,350 and 1,430–1,450 cm^{-1} , which are resolved in the spectra where the masking peaks of the coadsorbed carboxylate are suppressed (SI Appendix, section S4 and Figs. S19C, S20, and S21). Noteworthy is that earlier SEIRAS studies have assigned the high-frequency $\nu_3\text{C-O}$ vibration of adsorbed carbonate to a peak at $\sim 1,540\text{ cm}^{-1}$, which is most pronounced at potentials anodic of the electrocatalytic region (30–32, 35). This peak is also observed by SERS (Fig. 2 and SI Appendix, Figs. S11, S13, and S15). However, as discussed in detail in SI Appendix, section S4, we rule out this assignment because the 1,540- cm^{-1} peak is suppressed under certain conditions while the accompanying $\nu_1\text{CO}_3^{2-}$ peak at 1,065 cm^{-1} remains prominent (SI Appendix, Figs. S19–S21). In addition, the carbonate origin of the 1,540- cm^{-1} peak is in apparent conflict with the ^{13}C shift and the spectral properties of the $\nu_1\text{CO}_3^{2-}$ peak. We assign the 1,540- cm^{-1} peak to the coadsorbed carboxylate in *Carboxylate*.

As of now, carbonate adsorption on the metals that are active in CO_2 reduction is poorly understood. Since carbonate is a hard base, it is anticipated to form mostly ionic (electrostatic) bonds with the metal. The most straightforward pathway to form such a bond is through ligand exchange of HCO_3^- with adsorbed water/hydroxyl followed by deprotonation (38, 52). Alternatively, $\eta^1\text{-CO}_3^{2-}$ can be formed by activation of CO_2 on the surface oxygen/ OH^- sites or $^*\text{CO}_2^-$ (the Freund–Messmer mechanism) (46, 48, 49, 53), suggesting that $\eta^1\text{-CO}_3^{2-}$ and $^*\text{CO}_2^-$ establish surface equilibrium. Carbonate adsorption can be stabilized by surface defects (53). The break in the Stark tuning rate of the carbonate peak in the electrocatalytic region can be attributed to a decrease in the local surface concentration of $\eta^1\text{-CO}_3^{2-}$ by negative surface charge and hydrogen adsorption. A decrease in the local surface concentration of randomly adsorbed dipoles pulls their collective vibrational frequency down because it makes their dipole–dipole coupling weaker (54).

Obviously, further experimental and DFT studies are required to shed light on the carbonate adsorption on CO_2 electroreduction catalysts.

Carboxylate. In the context of the CO_2 electroreduction, of particular interest are peaks at $\sim 1,540$ and 350 cm^{-1} , which are best resolved at potentials from -0.3 to -0.9 V (Fig. 2 and SI Appendix, Figs. S11, S13, and S15). These peaks also persist at potentials cathodic of approximately -0.9 V where the Cu surface synthesizes formate (SI Appendix, Fig. S8), albeit the 350- cm^{-1} peak has a very low signal-to-noise ratio of 2–3 (Fig. 2, Insets and SI Appendix, Fig. S11, Insets). The 1,540- cm^{-1} peak has earlier been assigned to adsorbed carbonate (30–32, 35). We confidently discard this assignment in view of the arguments presented in SI Appendix, section S4. In the following, we prove that the 1,540 and 350- cm^{-1} peaks are vibrational fingerprints of $\eta^2(\text{C},\text{O})\text{-CO}_2^-$ (Fig. 1).

Before we proceed further, we should mention that the 1,540- cm^{-1} peak falls into the characteristic frequency range not only of the high-

frequency $\nu_3\text{C-O}$ vibration of carbonate complexes, but also the asymmetric C–O stretching vibration, $\nu_{\text{as}}\text{CO}_2^-$, of carboxylates (17, 48, 49, 55), while the 350- cm^{-1} peak is in the frequency range of the adsorbate–surface vibrations (17, 48).

Our first important finding is that the 1,540- cm^{-1} peak correlates with the 350- cm^{-1} peak in all of the spectral sets acquired (Fig. 3D and SI Appendix, Figs. S12D, S14D, S15, S19C, S20, and S21). Moreover, intensities and positions of these two peaks always change with potential in concert. Of particular importance is that breaks in their dependences are always observed at the same potential. For example, in Fig. 3 C and D, intensities of both the peaks increase as potential is scanned from -0.3 to -0.7 V, decreasing at more cathodic potentials. Similarly, the peak positions change marginally at potentials from -0.3 to -0.5 V and red shift at potentials from -0.5 to -0.9 V. A concerted response to a stimulus (in our case, electrode potential) is the main criterion used to discriminate peaks of the same species from a crowded spectrum (56). On this ground, we conclude that the 1,540 and 350- cm^{-1} peaks characterize the same species.

The second important result is that both these peaks are significantly suppressed in Ar-saturated 0.05 M Na_2CO_3 (pH 11.5) (SI Appendix, Fig. S21). Under these conditions, the theoretical concentration of dissolved CO_2 is as low as 0.02 μM , much lower than 33 mM in CO_2 -saturated 0.1 M NaHCO_3 . This result suggests that the 1,540 and 350- cm^{-1} peaks characterize activated CO_2 rather than adsorbed carbonate.

In the next step, we exclude all hypothesized protonated species from the picture (Fig. 1). The rationale is the negligible impact of the $\text{D}_2\text{O}/\text{H}_2\text{O}$ isotope exchange on the whole spectra, including the 1,540- cm^{-1} peak (Fig. 4B and SI Appendix, Fig. S16). Notable is the 1,200- to 1,400- cm^{-1} region characteristic of the C–OH stretching and HO–C bending peaks of $^*\text{COOH}$ (37, 57). Hence, the available options narrow down to carboxylates.

Another key result is that both the 1,540- and 350- cm^{-1} peaks red shift in $^{13}\text{CO}_2$ -saturated $\text{NaH}^{13}\text{CO}_3$ by a factor of 1.026 ± 0.002 (Fig. 4A and SI Appendix, Fig. S17A). Hence, these two peaks are not due to any contamination. The shift of the 1,540- cm^{-1} peak is more compatible with $\nu_{\text{as}}\text{CO}_2^-$ of carboxylate than $\nu_3\text{C-O}$ of carbonate. In fact, the ^{13}C shift factor of 1.026 ± 0.002 is comparable to 1.029 and 1.027 observed for $\nu_{\text{as}}\text{CO}_2^-$ of sodium acetate (58) and $\text{CO}_2^{\bullet-}$ in a Ne matrix (59), respectively, but lower than 1.033 observed for the high-frequency $\nu_3\text{CO}_3^-$ vibration of HCO_3^- in water (60). This relationship is in line with a notion that the C–O stretching vibration that involves a carbon atom connected to two oxygen atoms is typically less affected by the $^{13}\text{C}/^{12}\text{C}$ exchange than that when a carbon atom connected to three oxygen atoms (60). The ^{13}C effect on the 350- cm^{-1} peak indicates that the carboxylate is attached to the surface through the C atom. Hence, the $^{13}\text{C}/^{12}\text{C}$ isotope exchange leaves only the $\eta^1(\text{C})\text{-CO}_2^-$ and $\eta^2(\text{C},\text{O})\text{-CO}_2^-$ carboxylates for further consideration (Fig. 1).

Finally, the $\nu_{\text{as}}\text{CO}_2^-$ character of the 1,540- cm^{-1} peak rules out the $\eta^1(\text{C})\text{-CO}_2^-$ structure (C_{2v} symmetry). Its $\nu_{\text{as}}\text{CO}_2^-$ vibrational dipole is parallel to the surface. According to the surface selection rules, such a dipole would be strongly suppressed in SERS and silent in SEIRAS, in apparent contradiction with what is observed in Fig. 2 and SI Appendix, Figs. S11, S13, and S15 and refs. 30–32, 35. The same token supports the above rejection of $\eta^2(\text{O},\text{O})\text{-CO}_2^-$.

Thus, the only species left from the hypothesized set (Fig. 1) is $\eta^2(\text{C},\text{O})\text{-CO}_2^-$. On this basis, we assign the 1,540- and 350- cm^{-1} peaks to the $\nu_{\text{as}}\text{CO}_2^-$ and $\nu_{\text{Cu-C}}$ vibrations of $\eta^2(\text{C},\text{O})\text{-CO}_2^-$, respectively. The $\nu_{\text{as}}\text{CO}_2^-$ vibration presents mostly stretching of the C–O bond that points out of the surface, while $\nu_{\text{Cu-C}}$ is mostly stretching of the Cu–C bond (SI Appendix, Fig. S22). This peak assignment is corroborated by the dependence of these peaks intensities on potential (see below and *Effect of cathodic potential*), as well as by the DFT simulations [*DFT Model of CO_2 Activation on Cu(111)*]. The $\nu_{\text{as}}\text{CO}_2^-$ frequency of 1,515–1,545 cm^{-1} of $\eta^2(\text{C},\text{O})\text{-CO}_2^-$ is significantly lower than 1,658 cm^{-1} of $\text{CO}_2^{\bullet-}$ radical in a Ne matrix

(59). Given that the red shift of the $\nu_{\text{as}}\text{CO}_2^-$ vibrational mode correlates with the activation and charge density on a CO_2 molecule (61), this fact suggests that the carboxylate is adsorbed strongly and bears a substantial negative charge, which also agrees with the DFT data.

The Stark tuning rate of the 1,540- and 350- cm^{-1} peaks is +25–65 and +25 \pm 2 cm^{-1}/V , respectively (Fig. 3 C and D and *SI Appendix*, Figs. S12 C and D, S14 C and D, and S15). Its positive sign indicates that the dipole moments of the corresponding vibrations are parallel to the negative electric field. This alignment is evident for the non-coordinated C–O bond and hence $\nu_{\text{as}}\text{CO}_2^-$ of $\eta^2(\text{C},\text{O})\text{-CO}_2^-$ (scheme in Fig. 3C). For the Cu–C bond, the parallel alignment is predicted by DFT in the next section (scheme in Fig. 3D). The positive Stark tuning rate also excludes carbon monoxide $^*\text{CO}$ as a possible origin of the 350- cm^{-1} peak because the rate of the metal–C vibration of $^*\text{CO}$ is always negative (from –6 to –20 cm^{-1}/V) (45, 62). Additional evidence of a non-CO origin of the 350- cm^{-1} peak is provided by the absence of the νCO peak of $^*\text{CO}$ at potentials from –0.3 to –0.7 V where the 350- cm^{-1} peak is most pronounced (Fig. 2 and *SI Appendix*, Figs. S11 and S13).

The symmetric stretching $\nu_s\text{CO}_2^-$ and in-plane bending δCO_2^- vibrations of $\eta^2(\text{C},\text{O})\text{-CO}_2^-$ can be associated with weak peaks at ~1,330 and 700 cm^{-1} , respectively (Fig. 2). The main argument is that their intensities correlate with intensities of the carboxylate peaks at 1,540 and 350 cm^{-1} rather than the carbonate peak at 1,065 cm^{-1} (*SI Appendix*, Fig. S15). The $\nu_s\text{CO}_2^-$ vibration presents mostly stretching of the C–O bond coordinated to the surface, while δCO_2^- presents an umbrella-like movement of the oxygen atoms (*SI Appendix*, Fig. S22). Hence, dipoles of these two vibrations are almost parallel to the surface, which can explain the low intensity of their SERS peaks. Accordingly, the $^{13}\text{C}/^{12}\text{C}$ isotope exchange red shifts the 1,330- cm^{-1} peak by a factor of 1.013 ± 0.003 , while the 700- cm^{-1} peak remains intact (Fig. 4A). It should be noted that these two peaks overlap with the $\nu_3\text{C-O}$ and δCO_2^- peaks of coadsorbed $\eta^1\text{-CO}_3^{2-}$, respectively (*SI Appendix*, Fig. S19C).

The proposed assignment of the carboxylate peaks is in good agreement with literature data for alkali metal- CO_2^- and macrocycle- CO_2^- adducts, as well as for $^*\text{CO}_2^-$ formed on metals and metal oxides from gas phase (16, 17, 48, 49, 63–66). In particular, the $\nu_{\text{as}}\text{CO}_2^-$ and $\nu_s\text{CO}_2^-$ peaks of $^*\text{CO}_2^-$ on transition metals have been reported at 1,530–1,660 and 1,130–1,350 cm^{-1} , respectively, while its δCO_2^- peak, at 650–820 cm^{-1} (16, 17, 48). The $^*\text{CO}_2^-$ formed from gas phase on CuO nanoparticles and supported Cu has been associated with peaks at ~1,535 and 1,210 cm^{-1} (64, 65). Peaks at 1,529–1,520 and 1,347–1,310 cm^{-1} characterize CO_2 activated on a Co(I) macrocycle in wet acetonitrile (66). In addition, there is a good match between the $\nu_{\text{as}}\text{CO}_2^-$, δCO_2^- , and $\nu\text{Cu-C}$ frequencies of $\eta^2(\text{C},\text{O})\text{-CO}_2^-$ and their values predicted by DFT [*DFT Model of CO_2 Activation on Cu(111)* and *SI Appendix*, section S6].

Finally, we should mention an array of small peaks, which evolves in the electrocatalytic region of potentials (cathodic of –0.8 V) (Fig. 2). These peaks are practically immune to the $\text{D}_2\text{O}/\text{H}_2\text{O}$ isotope exchange (Fig. 4B and *SI Appendix*, Fig. S16). At the same time, some of them (e.g., a peak at 1,600–1,690 cm^{-1}) red shift by the $^{13}\text{C}/^{12}\text{C}$ isotope exchange (Fig. 4A and *SI Appendix*, Fig. S17), indicating that the corresponding vibrations involve carbon. Accurate assignment of these peaks calls for a separate detailed study.

The proposed assignment of the main peaks is summarized in Table 1.

Effect of cathodic potential. At –0.1 V, the Cu surface is almost completely passivated by Cu(I)/Cu(II) oxides, which are characterized by a typical doublet at ~535 and 608 cm^{-1} (33, 67) (Fig. 2). At –0.3 V, these oxides are partially reduced, as follows from a decrease in the doublet intensity. Concomitantly, distinct peaks of $\eta^2(\text{C},\text{O})\text{-CO}_2^-$ at 1,540 and 350 cm^{-1} and of $\eta^1\text{-CO}_3^{2-}$ at 1,065 cm^{-1} pop up. As potential is biased further, intensity of the $\eta^2(\text{C},\text{O})\text{-CO}_2^-$ peaks increases and reaches maximum at approximately –0.7 V (Fig. 3 C

Table 1. Assignment of vibrational peaks of adsorbates formed on the Cu electrode in a CO_2 -saturated bicarbonate electrolyte

Frequency, cm^{-1}	Assignment
340–350	$\nu\text{Cu-C}$ of $\eta^2(\text{C},\text{O})\text{-CO}_2^-$
610 and 530–535	$\nu\text{Cu-O}$ of Cu(I)/Cu(II) oxides
703	In-plane δCO_2^- of $\eta^2(\text{C},\text{O})\text{-CO}_2^-$
1,070–1,060	$\nu_1\text{CO}_3^{2-}$ of $\eta^1\text{-CO}_3^{2-}$
1,330	$\nu_s\text{CO}_2^-$ of $\eta^2(\text{C},\text{O})\text{-CO}_2^-$
1,350–1,430	$\nu_3\text{C-O}$ of $\eta^1\text{-CO}_3^{2-}$
1,540–1,520	$\nu_{\text{as}}\text{CO}_2^-$ of $\eta^2(\text{C},\text{O})\text{-CO}_2^-$
2,074–2,060	νCO of $^*\text{CO}$ on atop sites

and D). This point coincides with the potential where intensity of the oxide doublet ceases to decrease further (Fig. 2), which is reproduced in the other sets (*SI Appendix*, Figs. S11, S13, and S15). Hence, the surface coverage of $\eta^2(\text{C},\text{O})\text{-CO}_2^-$ increases mostly due to the generation of the adsorption sites by reduction of the blocking oxides.

The found formation of $\eta^2(\text{C},\text{O})\text{-CO}_2^-$ at potentials much more anodic than the onset of the CO_2 electroreduction current is a very interesting phenomenon. Given that our Cu surface is highly defective and partially oxidized, this finding strongly supports the emerging understanding that the CO_2 activation can be enabled by cooperative effects from the surface defects and/or residual oxygen (68–71), as well as coadsorbed electron donors such as water (69) or hydroxyls. It is also in line with the well-established fact that $^*\text{CO}_2^-$ can be formed on partially reduced metal oxides from gas phase (49, 65) and on heteroaromatic macrocycles in solution (20, 66). This reaction is commonly attributed to the CO_2 activation at a Lewis pair where a partially reduced metal cation serves as an electron donor, while the Lewis acid stabilizes the oxygen atom (72) [*DFT Model of CO_2 Activation on Cu(111)*]. The $\eta^2(\text{C},\text{O})\text{-CO}_2^-$ formation at anodic potentials is also consistent with its spontaneous formation predicted by DFT on free and oxide-supported Cu^0 clusters (72, 73), as well as its large binding energy of –2.16 eV on Cu(111) in the presence of coadsorbed cation [*DFT Model of CO_2 Activation on Cu(111)*].

As potential is scanned from –0.7 to approximately –1.0 V, intensities of the $\eta^2(\text{C},\text{O})\text{-CO}_2^-$ peaks go down (Fig. 3 C and D), which can be attributed to a slow takeoff of the $\eta^2(\text{C},\text{O})\text{-CO}_2^-$ conversion to formate. This interpretation is supported by a small reduction peak observed in this potential range in the first CV (*SI Appendix*, Fig. S7B) and the traces of formate detected in the electrolyte by NMR at –0.95 V. The decrease in the peak intensities in this potential range is qualitatively consistent with the reaction rate being controlled by the second step as proposed recently on the basis of Tafel slopes for the CO synthesis on Au and Ag (74). However, this conclusion needs to be tested by a rigorous study of the reaction kinetics on the Cu surfaces that are sufficiently catalytically active in this potential range.

In the potential range from –0.3 to –1.0/–0.9 V, the C–O and Cu–C bonds of $\eta^2(\text{C},\text{O})\text{-CO}_2^-$ are gradually activated (become weaker), as concluded from the red shifts of its $\nu_{\text{as}}\text{CO}_2^-$ and $\nu\text{Cu-C}$ peaks (*SI Appendix*, section S5). The activation can be accounted for by the electrostatic and chemical effects induced by a negative surface charge [*DFT Model of CO_2 Activation on Cu(111)*].

The pattern changes qualitatively at –1.1 V in Fig. 3 C and D and at –0.9 V in *SI Appendix*, Fig. S14 C and D. Here, intensities of the carboxylate peaks drop dramatically and afterward slowly decrease (*SI Appendix*, Fig. S14 C and D). This new pattern perfectly complies with a CO_2 reduction reaction where the RDS is the $\eta^2(\text{C},\text{O})\text{-CO}_2^-$ formation [I] as suggested by the Tafel analysis (*SI Appendix*, Fig. S8B). Under these conditions, $\eta^2(\text{C},\text{O})\text{-CO}_2^-$ is expected to occupy only a minute fraction of surface sites, which explains the low intensities of the carboxylate peaks. Even though a further cathodic bias increases the formation rate of $\eta^2(\text{C},\text{O})\text{-CO}_2^-$,

its surface concentration remains low due to its fast consumption in the second step [4a] and [4b].

Thus, the effect of potential is fully consistent with the status of $\eta^2(\text{C,O})\text{-CO}_2^-$ as the first intermediate. The lag between the CO_2 activation and the activation followed by the second reaction step provides an exciting opportunity to study spectroscopically factors that promote the first and second step of the CO_2 reduction to formate and CO, as well as to uncover the nature of the second step of these two reactions.

DFT Model of CO_2 Activation on Cu(111). To verify the SERS results and assist in their interpretation, we model the CO_2 activation on Cu(111) using a plane wave DFT method (see *SI Appendix* for detail). In agreement with prior theoretical (21, 69, 75) and experimental (46, 76) works, we find that clean Cu(111) does not activate CO_2 (Fig. 5A). This can be explained by the relatively high work function of Cu and the low position of its d-band with respect to the Fermi level.

In the next computational experiment, we place a relaxed Na^+ cation hydrated by eight water molecules on the top of the linear CO_2 molecule relaxed over Cu(111) (Fig. 5A). This system is dubbed as $(\text{CO}_2+\text{Na}+8\text{H}_2\text{O})/\text{Cu}(111)$ hereafter. In this case, CO_2 is activated (Fig. 5B), adopting the $\eta^2(\text{C,O})\text{-CO}_2^-$ geometry, in unison with the SERS results. The CO_2 activation makes both the C–O bonds longer than in linear CO_2 , the effect being much more pronounced for the surface coordinated C–O bond, while the O–C–O angle decreases to 119° . This species has a relatively large binding energy of -2.16 eV, which indicates that in the presence of the cation CO_2 interacts with the Cu surface strongly. The promoting effect of alkali metals on the CO_2 activation on metal surfaces has earlier been attributed to a decrease in the metal work function (46, 75–78) and electric polarization of adsorbed carboxylate by the cation (24).

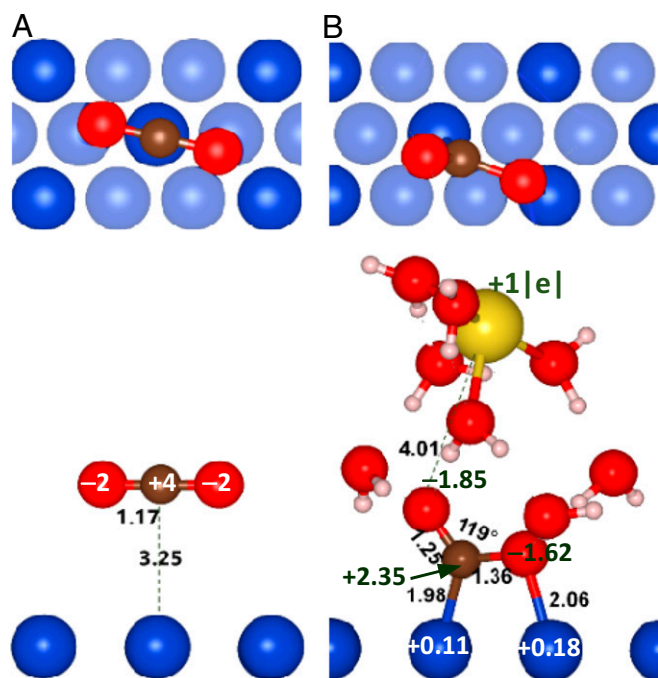


Fig. 5. Top and side views of the optimized structures of CO_2 on Cu(111) (A) linear physisorbed CO_2 and (B) $\eta^2(\text{C,O})\text{-CO}_2^-$ stabilized by Na^+ hydrated with eight water molecules, $(\text{CO}_2+\text{Na}+8\text{H}_2\text{O})/\text{Cu}(111)$. Bond lengths and angles are in angstroms and degrees, respectively. Bader charges of atoms are in $|e|$ units. Atom color codes: dark blue, Cu; red, oxygen; brown, carbon; yellow, sodium. The subsurface Cu atoms are shown in the top views as transparent blue spheres. Hydrated Na^+ is removed from the top view (B) to show the coordinating Cu atoms.

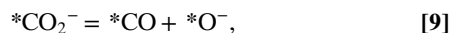
The predicted vibrational frequencies of $\eta^2(\text{C,O})\text{-CO}_2^-$ are in good agreement with the experimental values (*SI Appendix*, Table S2). In particular, the theoretical $\nu_{\text{as}}\text{CO}_2^-$ and $\nu_{\text{Cu-C}}$ frequencies of $1,503$ and 356 cm^{-1} are close to the experimental values of $1,515$ – $1,525$ and 345 cm^{-1} in the electrocatalytic region, respectively (Fig. 3 C and D and *SI Appendix*, Figs. S12 C and D, S14 C and D, and S15). The only exception is the $\nu_{\text{s}}\text{CO}_2^-$ vibration, which is predicted to be at ~ 970 cm^{-1} vs. $1,330$ cm^{-1} observed experimentally at anodic potentials. This discrepancy can tentatively be attributed to limitations of DFT in general and our DFT methodology in particular in modeling stretching vibrations of a molecular bond that is strongly coordinated parallel to the surface (see *SI Appendix* for more detail).

The $\eta^2(\text{C,O})\text{-CO}_2^-$ configuration is most popular in molecular complexes of CO_2 (16). It also has earlier been predicted for CO_2 activated on low-index Cu surfaces either by a bias force or alkali metal placed directly on the surface, on-side of CO_2 (24, 75). Our result is that $\eta^2(\text{C,O})\text{-CO}_2^-$ forms an ionic pair with a hydrated alkali metal cation located above the adsorbed anion. In addition to the electrolyte cations coadsorbed on side, a cation coordinated on top is likely to constitute the local environment of the anion adsorbed at a negatively charged electrode surface. The position of the cation is important for a better understanding of the CO_2 activation process, especially the promoting effects of cations and the role of hydrating water molecules (H-bonding) (79–82).

The Bader charge analysis (Fig. 5B and *SI Appendix*, Table S1) shows that activated CO_2 gains a net charge of $-1.12|e|$, that is, close to one electron, while the C atom gains $-1.65|e|$. The difference is explained by the depletion of the negative charge on the O atoms, especially the O atom coordinated to the surface (it loses $-0.38|e|$). This effect is caused by donation of π electrons of CO_2 to the surface (see below). In parallel, the Cu atoms in the Cu–C and Cu–O bonds acquire positive charges of $+0.11|e|$ and $+0.15|e|$, respectively, which additionally stabilize the adsorbed anion electrostatically.

To interpret the Bader charges, we compare $\eta^2(\text{C,O})\text{-CO}_2^-$ with free $\text{CO}_2^{\bullet-}$ anion radical, which is simulated as a CO_2+Na pair (without surface). In contrast to $\eta^2(\text{C,O})\text{-CO}_2^-$, all of the atoms in $\text{CO}_2^{\bullet-}$ gain negative charge (*SI Appendix*, Table S1). It follows that the O atoms in $\eta^2(\text{C,O})\text{-CO}_2^-$ are less basic than in $\text{CO}_2^{\bullet-}$, which makes them less susceptible to the electrophilic attack including protonation to $^*\text{COOH}$. Hence, reaction [2] is very unlikely on Cu at neutral pH, given that COOH^{\bullet} (protonated $\text{CO}_2^{\bullet-}$) is rather acidic [its experimental pK_a values are as low as 1.4 – 3.4 (83, 84)]. This result can explain the absence of carboxyls $^*\text{COOH}$ on the Cu surface in a SERS-detectable amount.

The lower basicity of $\eta^2(\text{C,O})\text{-CO}_2^-$ can also imply that, instead of previously proposed reaction [3], CO is produced on Cu through the direct dissociation of the carboxylate:



as observed in gas phase (46, 48) and proposed for CO_2 electroreduction by Ikeda et al. (85). Of particular interest is that pathway [9] dynamically supplies adsorbed oxygen, which is known to promote both the CO_2 activation and reduction (69).

In general, activation of CO_2 on transition metals is described as an acid–base process where the molecule accepts electron density on its lowest unoccupied molecular orbital (LUMO) and simultaneously donates electron from its highest occupied molecular orbital (HOMO) to an empty d orbital of the coordinating metal (16, 17, 48). The particular the d states involved depend on the metal and structure of the coordinating site(s). The frontier orbitals of bent CO_2 , which are represented by the corresponding molecular orbitals of $\text{CO}_2^{\bullet-}$, are shown in Fig. 6A. The LUMO presents the antibonding $6a_1$ (in-plane) orbital, which descends from the degenerate anti-bonding $2\pi_u^*$ LUMO of linear CO_2 . It is heavily centered on the carbon atom. According to our density of states calculations, it presents a mix of 33% C 2p and 9% C 2s with 26%

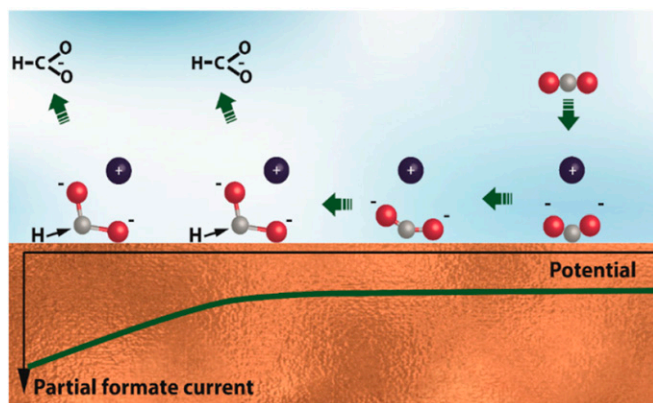


Fig. 7. Proposed model of CO₂ activation on a Cu electrode in aqueous electrolyte. $\eta^2(\text{C,O})\text{-CO}_2^-$ is formed at potentials anodic of the electrocatalytic current. Cathodic polarization gradually activates this species (elongates the C–O bonds and decreases the O–C–O angle), which is accompanied by weakening of its Cu–C bond and stabilization of the Cu–O bond. The electrocatalytic reaction starts when $\eta^2(\text{C,O})\text{-CO}_2^-$ is able to participate in the second electron transfer, for example, to react with $^*\text{H}$ to produce formate. Atom colors: red, oxygen; gray, carbon.

this Cu atom is polarized away from the Cu–C bond. This charge redistribution indicates repulsive interactions, which make the Cu–C bond more ionic. A similar conclusion has been derived for CO₂/Pt(110) based on the direct effect of the electric field (87). The increased ionic character of the Cu–C bond of $\eta^2(\text{C,O})\text{-CO}_2^-$ at a more negatively charged surface suggests that this bond is activated. This effect can make feasible a nucleophilic attack at the C atom by hydrogen.

In contrast, the Cu atom of the Cu–O bond accumulates d_{z^2} electron density symmetrically, with the lobe expanding toward the O atom (Fig. 6D). Hence, the Cu–O bond can be stabilized by a negative potential, which can drive the dissociation of $\eta^2(\text{C,O})\text{-CO}_2^-$ [9]. Given that the Cu–C bond can be concomitantly destabilized, this feature makes the metal–oxygen bond essential for the stabilization and function of $\eta^2(\text{C,O})\text{-CO}_2^-$ as the first intermediate.

Our SERS and DFT results on CO₂ activation are summarized in Fig. 7.

Conclusions

By applying a comprehensive suite of experimental and theoretical methods, we establish that the CO₂ conversion to formate on Cu starts with the formation of a carboxylate intermediate with the $\eta^2(\text{C,O})\text{-CO}_2^-$ structure. This result can be generalized toward at least coinage metals (Cu, Au, and Ag), given their similarity in terms of the reaction kinetics and the electronic properties. At the same time, the formation of $^*\text{COOH}$ is unlikely on Cu at circumneutral and basic pH, which implies that $\eta^2(\text{C,O})\text{-CO}_2^-$ is converted to CO through direct dissociation [9] as in gas phase.

$\eta^2(\text{C,O})\text{-CO}_2^-$ is stabilized on a Cu surface due to the strong covalency of its two bonds with the surface, charge polarization in the system, as well as by the electrostatic interactions with a hydrated Na cation in the on-top position and the positively charged coordinating Cu atoms. The observed formation of $\eta^2(\text{C,O})\text{-CO}_2^-$ at potentials much more anodic of the onset of the CO₂ electroreduction suggests the critical role of additional cooperative effects such as surface defects, residual surface oxide, and coadsorbed electron donors, which are yet to be understood. A negative potential activates the Cu–C and C–O bonds of $\eta^2(\text{C,O})\text{-CO}_2^-$ en route to HCOO[−] (Fig. 7), which is explained by the electrostatic and chemical effects. In contrast, the Cu–O bond can be stabilized, underscoring its important role in the selectivity of $\eta^2(\text{C,O})\text{-CO}_2^-$ to CO and HCOO[−].

These results indicate that the descriptors of the CO₂ conversion to HCOO[−] and CO are the chemical and structural properties of $\eta^2(\text{C,O})\text{-CO}_2^-$, raising intriguing questions about the exact relationship of these properties to the selectivity, activity, and energy efficiency of the catalyst.

ACKNOWLEDGMENTS. We thank Prof. Bob Farrauto for sharing a micro-GC instrument, Dr. Qinghe (Angela) Zheng for initial technical support of the micro-GC measurements, as well as the anonymous reviewers for their suggestions and corrections. This research was enabled in part by computational support provided by Compute Canada. I.V.C. and P.S. acknowledge funding support from the National Science Foundation under Award 1336845 as well as through the Industry/University Cooperative Research Center's Center for Particulate and Surfactant Systems (IIP-0749461). S.P. acknowledges the support from Chemical and Petroleum Engineering, Canada First Research Excellence Fund at University of Calgary, and Natural Sciences and Engineering Research Council of Canada Discovery Grant RGPIN-2016-03851.

- Tatin A, Bonin J, Robert M (2016) A case for electrofuels. *ACS Energy Lett* 1: 1062–1064.
- Spurgeon J, Kumar B (2018) A comparative techno-economic analysis of pathways for commercial electrochemical CO₂ reduction to liquid products. *Energy Environ Sci* 11: 1536–1551.
- Goldsmith BR, Esterhuizen J, Bartel CJ, Sutton C, Liu JX (2018) Machine learning for heterogeneous catalyst design and discovery. *AIChE J* 64:2311–2323.
- Liu X, et al. (2017) Understanding trends in electrochemical carbon dioxide reduction rates. *Nat Commun* 8:15438.
- Feaster JT, et al. (2017) Understanding selectivity for the electrochemical reduction of carbon dioxide to formic acid and carbon monoxide on metal electrodes. *ACS Catal* 7: 4822–4827.
- Akhade SA, Luo WJ, Nie XW, Asthagiri A, Janik MJ (2016) Theoretical insight on reactivity trends in CO₂ electroreduction across transition metals. *Catal Sci Technol* 6: 1042–1053.
- Hori Y (2008) Electrochemical CO₂ reduction on metal electrodes. *Modern Aspects of Electrochemistry*, eds Vayenas CG, White RE, Gamboa-Aldeco ME (Springer, New York), Vol 2, pp 89–189.
- Hori Y, Wakebe H, Tsukamoto T, Koga O (1994) Electrocatalytic process of CO selectivity in electrochemical reduction of CO₂ at metal electrodes in aqueous media. *Electrochim Acta* 39:1833–1839.
- Gattrell M, Gupta N, Co A (2006) A review of the aqueous electrochemical reduction of CO₂ to hydrocarbons at copper. *J Electroanal Chem* 594:1–19.
- Jitaru M, Lowy DA, Toma M, Toma BC, Oniciu L (1997) Electrochemical reduction of carbon dioxide on flat metallic cathodes. *J Appl Electrochem* 27:875–889.
- Noda H, Ikeda S, Yamamoto A, Einaga H, Ito K (1995) Kinetics of electrochemical reduction of carbon-dioxide on a gold electrode in phosphate buffer solutions. *Bull Chem Soc Jpn* 68:1889–1895.
- Li CW, Kanan MW (2012) CO₂ reduction at low overpotential on Cu electrodes resulting from the reduction of thick Cu₂O films. *J Am Chem Soc* 134:7231–7234.
- Chen Y, Li CW, Kanan MW (2012) Aqueous CO₂ reduction at very low overpotential on oxide-derived Au nanoparticles. *J Am Chem Soc* 134:19969–19972.
- Wuttig A, Yaguchi M, Motobayashi K, Osawa M, Surendranath Y (2016) Inhibited proton transfer enhances Au-catalyzed CO₂-to-fuels selectivity. *Proc Natl Acad Sci USA* 113:E4585–E4593.
- Verma S, et al. (2018) Insights into the low overpotential electroreduction of CO₂ to CO on a supported gold catalyst in an alkaline flow electrolyzer. *ACS Energy Lett* 3: 193–198.
- Aresta M, Angelini A (2016) The carbon dioxide molecule and the effects of its interaction with electrophiles and nucleophiles. *Carbon Dioxide and Organometallics*, Topics in Organometallic Chemistry, ed Lu XB (Springer, New York), Vol 53, pp 1–38.
- Gibson DH (1999) Carbon dioxide coordination chemistry: Metal complexes and surface-bound species. What relationships? *Coord Chem Rev* 185–186:335.
- Chaplin RPS, Wragg AA (2003) Effects of process conditions and electrode material on reaction pathways for carbon dioxide electroreduction with particular reference to formate formation. *J Appl Electrochem* 33:1107–1123.
- Kortlever R, Shen J, Schouten KJP, Calle-Vallejo F, Koper MTM (2015) Catalysts and reaction pathways for the electrochemical reduction of carbon dioxide. *J Phys Chem Lett* 6:4073–4082.
- Schouten KJ, Koper M (2013) Key intermediates in the hydrogenation and electrochemical reduction of CO₂. *Photoelectrochemical Water Splitting: Materials, Processes and Architectures*, RSC Energy and Environment Series, eds Lewerenz HJ, Peter L (Royal Society of Chemistry, London), pp 333–358.
- Ko J, Kim B-K, Han JW (2016) Density functional theory study for catalytic activation and dissociation of CO₂ on bimetallic alloy surfaces. *J Phys Chem C* 120:3438–3447.
- Cheng T, Xiao H, Goddard WA (2016) Reaction mechanisms for the electrochemical reduction of CO₂ to CO and formate on the Cu(100) surface at 298 K from quantum mechanics free energy calculations with explicit water. *J Am Chem Soc* 138: 13802–13805.

23. Nie XW, Luo WJ, Janik MJ, Asthagiri A (2014) Reaction mechanisms of CO₂ electrochemical reduction on Cu(111) determined with density functional theory. *J Catal* 312: 108–122.
24. Chen LD, Urushihara M, Chan KR, Nørskov JK (2016) Electric field effects in electrochemical CO₂ reduction. *ACS Catal* 6:7133–7139.
25. Cheng T, Huang Y, Xiao H, Goddard WA, 3rd (2017) Predicted structures of the active sites responsible for the improved reduction of carbon dioxide by gold nanoparticles. *J Phys Chem Lett* 8:3317–3320.
26. Durand WJ, Peterson AA, Studt F, Abild-Pedersen F, Nørskov JK (2011) Structure effects on the energetics of the electrochemical reduction of CO₂ by copper surfaces. *Surf Sci* 605:1354–1359.
27. Kortlever R, Tan KH, Kwon Y, Koper MTM (2013) Electrochemical carbon dioxide and bicarbonate reduction on copper in weakly alkaline media. *J Solid State Electrochem* 17:1843–1849.
28. Baruch MF, Pander JE, White JL, Bocarsly AB (2015) Mechanistic insights into the reduction of CO₂ on tin electrodes using in situ ATR-IR spectroscopy. *ACS Catal* 5: 3148–3156.
29. Wain AJ, O'Connell MA (2017) Advances in surface-enhanced vibrational spectroscopy at electrochemical interfaces. *Advances in Physics-X* 2:188–209.
30. Wuttig A, et al. (2016) Tracking a common surface-bound intermediate during CO₂-to-fuels catalysis. *ACS Cent Sci* 2:522–528.
31. Heyes J, Dunwell M, Xu BJ (2016) CO₂ reduction on Cu at low overpotentials with surface-enhanced in situ spectroscopy. *J Phys Chem C* 120:17334–17341.
32. Zhu S, Jiang B, Cai W-B, Shao M (2017) Direct observation on reaction intermediates and the role of bicarbonate anions in CO₂ electrochemical reduction reaction on Cu surfaces. *J Am Chem Soc* 139:15664–15667.
33. Smith BD, Irish DE, Kedzierzawski P, Augustynski J (1997) A surface enhanced Raman scattering study of the intermediate and poisoning species formed during the electrochemical reduction of CO₂ on copper. *J Electrochem Soc* 144:4288–4296.
34. Batista EA, Temperini MLA (2009) Spectroscopic evidences of the presence of hydrogenated species on the surface of copper during CO₂ electroreduction at low cathodic potentials. *J Electroanal Chem* 629:158–163.
35. Oda I, Ogasawara H, Ito M (1996) Carbon monoxide adsorption on copper and silver electrodes during carbon dioxide electroreduction studied by infrared reflection absorption spectroscopy and surface-enhanced Raman spectroscopy. *Langmuir* 12: 1094–1097.
36. Schmitt KG, Gewirth AA (2014) In situ surface-enhanced Raman spectroscopy of the electrochemical reduction of carbon dioxide on silver with 3,5-diamino-1,2,4-triazole. *J Phys Chem C* 118:17567–17576.
37. Fret NJ, Smith WA (2017) Probing the reaction mechanism of CO₂ electroreduction over Ag films via operando infrared spectroscopy. *ACS Catal* 7:606–612.
38. Chernyshova IV, Ponnurangam S, Somasundaran P (2013) Linking interfacial chemistry of CO₂ to surface structures of hydrated metal oxide nanoparticles: Hematite. *Phys Chem Chem Phys* 15:6953–6964.
39. Ponnurangam S, Chernyshova IV, Somasundaran P (2010) Effect of co-adsorption of electrolyte ions on the stability of inner-sphere complexes. *J Phys Chem C* 114: 16517–16524.
40. Kas R, et al. (2016) Three-dimensional porous hollow fibre copper electrodes for efficient and high-rate electrochemical carbon dioxide reduction. *Nat Commun* 7: 10748.
41. Ponnurangam S, Yun CM, Chernyshova IV (2016) Robust electroreduction of CO₂ at a poly(4-vinylpyridine)-copper electrode. *ChemElectroChem* 3:74–82.
42. Fried SD, Boxer SG (2015) Measuring electric fields and noncovalent interactions using the vibrational Stark effect. *Acc Chem Res* 48:998–1006.
43. Lowy DA, Jitaru M (2014) Electroreduction of carbon dioxide. *Electrochemically Enabled Sustainability: Devices, Materials and Mechanisms for Energy Conversion*, eds Chan K-Y, Li C-YV (CRC, Boca Raton, FL), pp 1–53.
44. Dederichs F, Friedrich KA, Daum W (2000) Sum-frequency vibrational spectroscopy of CO adsorption on Pt(111) and Pt(110) electrode surfaces in perchloric acid solution: Effects of thin-layer electrolytes in spectroelectrochemistry. *J Phys Chem B* 104: 6626–6632.
45. Zou SZ, Weaver MJ (1996) Potential-dependent metal-adsorbate stretching frequencies for carbon monoxide on transition-metal electrodes: Chemical bonding versus electrostatic field effects. *J Phys Chem* 100:4237–4242.
46. Pohl M, Otto A (1998) Adsorption and reaction of carbon dioxide on pure and alkali-metal promoted cold-deposited copper films. *Surf Sci* 406:125–137.
47. Santos VO, Leite IR, Brolo AG, Rubim JC (2016) The electrochemical reduction of CO₂ on a copper electrode in 1-*n*-butyl-3-methyl imidazolium tetrafluoroborate (BMI.BF₄) monitored by surface-enhanced Raman scattering (SERS). *J Raman Spectrosc* 47: 674–680.
48. Freund HJ, Roberts MW (1996) Surface chemistry of carbon dioxide. *Surf Sci Rep* 25: 225–273.
49. Seifert O, et al. (1999) IR investigations of CO₂ adsorption on chromia surfaces: Cr₂O₃(0001)/Cr(110) versus polycrystalline alpha-Cr₂O₃. *Surf Sci* 421:176–190.
50. Lukomska A, Sobkowski J (2004) Potential of zero charge of monocrystalline copper electrodes in perchlorate solutions. *J Electroanal Chem* 567:95–102.
51. Iwasita T, Rodes A, Pastor E (1995) Vibrational spectroscopy of carbonate adsorbed on Pt(111) and Pt(110) single-crystal electrodes. *J Electroanal Chem* 383:181–189.
52. Koga O, Watanabe Y, Tanizaki M, Hori Y (2001) Specific adsorption of anions on a copper (100) single crystal electrode studied by charge displacement by CO adsorption and infrared spectroscopy. *Electrochim Acta* 46:3083–3090.
53. Schumacher N, et al. (2008) Interaction of carbon dioxide with Cu overlayers on Pt(111). *Surf Sci* 602:702–711.
54. Ryberg R (1989) Infrared spectroscopy of molecules adsorbed on metal surfaces. *Advances in Chemical Physics* (Wiley, Chichester, UK), pp 1–44.
55. Busca G, Lorenzelli V (1982) Infrared spectroscopic identification of species arising from reactive adsorption of carbon oxides on metal-oxide surfaces. *Mater Chem* 7:89–126.
56. Tolstoy VP, Chernyshova IV, Skryshevsky VA (2003) *Handbook of Infrared Spectroscopy of Ultrathin Films* (Wiley, Hoboken, NJ).
57. Rotzinger FP, Kesselman-Truttmann JM, Hug SJ, Shklover V, Gratzel M (2004) Structure and vibrational spectrum of formate and acetate adsorbed from aqueous solution onto the TiO₂ rutile (110) surface. *J Phys Chem B* 108:5004–5017.
58. Kakihana M, Kotaka M, Okamoto M (1983) Vibrational analysis of acetate ion molecules and estimation of equilibrium-constants for their hydrogen isotopic exchange-reactions. *J Phys Chem* 87:2526–2535.
59. Thompson WE, Jacox ME (1999) The vibrational spectra of CO₂⁺, (CO₂)₂⁺, CO₂⁻, and (CO₂)₂⁻ trapped in solid neon. *J Chem Phys* 111:4487–4496.
60. Sheng H, et al. (2018) Carbon dioxide dimer dissociation as surface intermediate of photoinduced CO₂ reduction at aqueous Cu and CdSe nanoparticle catalysts by rapid-scan FT-IR spectroscopy. *J Am Chem Soc* 140:4363–4371.
61. Dodson LG, Thompson MC, Weber JM (2018) Characterization of intermediate oxidation states in CO₂ activation. *Annu Rev Phys Chem* 69:231–252.
62. Deshlahra P, Wolf EE, Schneider WF (2009) A periodic density functional theory analysis of CO chemisorption on Pt(111) in the presence of uniform electric fields. *J Phys Chem A* 113:4125–4133.
63. Onsgaard J, et al. (1995) The interaction of CO₂ with potassium-promoted Cu(110): Adsorption, reactions and radiation induced dissociation of CO₂. *Surf Sci* 336:101–112.
64. Weigel J, Koeppl RA, Baiker A, Wokaun A (1996) Surface species in CO and CO₂ hydrogenation over copper/zirconia: On the methanol synthesis mechanism. *Langmuir* 12:5319–5329.
65. Gankanda A, Cwierzny DM, Grassian VH (2016) Role of atmospheric CO₂ and H₂O adsorption on ZnO and CuO nanoparticle aging: Formation of new surface phases and the impact on nanoparticle dissolution. *J Phys Chem C* 120:19195–19203.
66. Sheng H, Frei H (2016) Direct observation by rapid-scan FT-IR spectroscopy of two-electron-reduced intermediate of tetraaza catalyst [Co⁰(N₄H(McCN))]⁽²⁺⁾ converting CO₂ to CO. *J Am Chem Soc* 138:9959–9967.
67. Chan HYH, Takoudis CG, Weaver MJ (1999) Oxide film formation and oxygen adsorption on copper in aqueous media as probed by surface-enhanced Raman spectroscopy. *J Phys Chem B* 103:357–365.
68. Garza AJ, Bell AT, Head-Gordon M (2018) Is subsurface oxygen necessary for the electrochemical reduction of CO₂ on copper? *J Phys Chem Lett* 9:601–606.
69. Favaro M, et al. (2017) Subsurface oxide plays a critical role in CO₂ activation by Cu(111) surfaces to form chemisorbed CO₂, the first step in reduction of CO₂. *Proc Natl Acad Sci USA* 114:6706–6711.
70. Cavalca F, et al. (2017) Nature and distribution of stable subsurface oxygen in copper electrodes during electrochemical CO₂ reduction. *J Phys Chem C* 121:25003–25009.
71. Jeon HS, et al. (2018) Operando evolution of the structure and oxidation state of size-controlled Zn nanoparticles during CO₂ electroreduction. *J Am Chem Soc* 140: 9383–9386.
72. Bal K, Huygh S, Bogaerts A, & Neyts E (2018) Effect of plasma-induced surface charging on catalytic processes: Application to CO₂ activation. *Plasma Sources Sci Technol* 27: 024001.
73. Rawat KS, Mahata A, Pathak B (2017) Thermochemical and electrochemical CO₂ reduction on octahedral Cu nanocluster: Role of solvent towards product selectivity. *J Catal* 349:118–127.
74. Dunwell M, Luc W, Yan Y, Jiao F, Xu B (2018) Understanding surface-mediated electrochemical reactions: CO₂ reduction and beyond. *ACS Catal* 8:8121–8129.
75. Ou LH, Chen YD, Jin JL (2016) Theoretical insights into the alkaline metal M (M = Na and Cs) promotion mechanism for CO₂ activation on the Cu(111) surface. *RSC Advances* 6:67866–67874.
76. Burghaus U (2014) Surface chemistry of CO₂—adsorption of carbon dioxide on clean surfaces at ultrahigh vacuum. *Prog Surf Sci* 89:161–217.
77. Ding X, et al. (2007) Interaction of carbon dioxide with Ni(110): A combined experimental and theoretical study. *Phys Rev B* 76:195425.
78. Wang S-G, et al. (2007) Factors controlling the interaction of CO₂ with transition metal surfaces. *J Phys Chem C* 111:16934–16940.
79. Resasco J, et al. (2017) Promoter effects of alkali metal cations on the electrochemical reduction of carbon dioxide. *J Am Chem Soc* 139:11277–11287.
80. Verma S, Lu X, Ma S, Masel RI, Kenis PJA (2016) The effect of electrolyte composition on the electroreduction of CO₂ to CO on Ag based gas diffusion electrodes. *Phys Chem Chem Phys* 18:7075–7084.
81. Thorson MR, Siil KI, Kenis PJA (2013) Effect of cations on the electrochemical conversion of CO₂ to CO. *J Electrochem Soc* 160:F69–F74.
82. Ambrosio RC, Gewirth AA (2010) Characterization of water structure on silver electrode surfaces by SERS with two-dimensional correlation spectroscopy. *Anal Chem* 82: 1305–1310.
83. Buxton GV, Sellers RM (1973) Acid dissociation-constant of carboxyl radical—Pulse-radiolysis studies of aqueous-solutions of formic-acid and sodium formate. *J Chem Soc Faraday Trans 1* 69:555–559.
84. Janik I, Tripathi GNR (2016) The nature of the CO₂⁻ radical anion in water. *J Chem Phys* 144:154307.
85. Ikeda S, Takagi T, Ito K (1987) Selective formation of formic-acid, oxalic-acid, and carbon-monoxide by electrochemical reduction of carbon-dioxide. *Bull Chem Soc Jpn* 60:2517–2522.
86. Liu C, Cundari TR, Wilson AK (2012) CO₂ reduction on transition metal (Fe, Co, Ni, and Cu) surfaces: In comparison with homogeneous catalysis. *J Phys Chem C* 116:5681–5688.
87. Gudmundsdóttir S, Tang W, Henkelman G, Jónsson H, Skúlason E (2012) Local density of states analysis using Bader decomposition for N₂ and CO₂ adsorbed on Pt(110)-(1 × 2) electrodes. *J Chem Phys* 137:164705.